Catalysis Science & **Technology**



View Article Online **PAPER**



Cite this: Catal. Sci. Technol., 2022, **12**, 5629

Received 29th March 2022 Accepted 29th July 2022

DOI: 10.1039/d2cy00602b

rsc.li/catalvsis

Computational screen of M₂P metal phosphides for catalytic ethane dehydrogenation†

Jeonghyun Ko^a and William F. Schneider (1)**ab

Metal phosphides are promising catalysts for hydrocarbon transformations, but computational screening is complicated by their diverse structures and compositions. To disentangle structural from compositional contributions, here we explore the metal-rich M₂P (M = Fe, Co, Ni, Cu, Mo, Ru, Rh, Pd, Ag, Pt) series in hexagonal and orthorhombic structures that are common to a subset of these materials, using supercell density functional theory (DFT). To understand the contribution of metal choice to utility for catalytic ethane dehydrogenation (EDH), we compute and compare the adsorption of key EDH intermediates across low-index surface terminations. These materials expose both metal and phosphide sites. Calculations show that binding energies at metal sites correlate with the bulk metals, with P incorporation either enhancing or suppressing binding. Phosphide sites compete with metal sites for adsorbates and tend to suppress overactivation by destabilizing highly dehydrogenated species engaging in C-H bond breaking. Results are generally insensitive to bulk structure and surface facet. Results suggest metal-rich Pd phosphides to have favorable adsorption characteristics for catalytic dehydrogenation, consistent with recent observations.

1 Introduction

The discovery of abundant shale resources in the United States has resulted in gas liquids (NGLs) production to exceed their domestic consumption. 1-4 Ethane is the most prevalent component of NGLs, and dehydrogenation to ethylene is the first step in converting into a petrochemical feedstock.³ Steam cracking of ethane is energy- and capital-intensive, 5,6 motivating the development of alternative and scalable dehydrogenation strategies.

Catalytic dehydrogenation of ethane $(C_2H_6 \rightarrow C_2H_4 + H_2)$ is an alternative option to steam cracking for ethylene production. Ethane dehydrogenation (EDH) could operate with smaller and local processing plants than steam cracking. However, temperatures greater than 750 °C are required to achieve ≥50% conversion at atmospheric pressure. Catalyst selectivity and resistance to coke are both challenging at these harsh conditions. EDH catalysis is not practiced commercially today.

Smaller active metal ensembles are known to be effective in mitigating side reactions and coke formation during catalytic EDH.7-11 Alloying a second metal (Sn,7-9 Zn,10 and In (ref. 11)) into Pt or Pd is observed to improve selectivity and catalyst stability. Similar to metal alloys, metal phosphides have been shown to offer potential as selective and robust EDH catalysts. 12-16 Recently, density functional theory (DFT) calculations, and spectroscopic and reaction measurements studies have shown that phosphorus addition into Ni (ref. 17) and Co (ref. 18) improves EDH selectivity and durability. A density functional theory (DFT) comparison of EDH performance on Ni(111) and Ni₂P(001)^{17,51} showed that P atoms selectively participate in adsorbate binding and C-H bond breaking, increasing activation barriers for steps leading to deep dehydrogenation and promoting ethylene desorption over ethylene overactivation. In addition, P incorporation weakens binding of small hydrocarbons, imparting coke resistance to the surface. These two features are predicted to contribute to the remarkable product selectivity and intrinsic EDH activity of Ni₂P.

While recent work has focused on Ni- and Co-based phosphides as alkane dehydrogenation catalysts, 17-22 other metal phosphides exhibit promising catalytic performance for other catalytic reactions. 12-16 Thus, an overall picture of EDH performance across metal phosphides is yet to be established. Because performance is closely linked to binding

^a Department of Chemical and Biomolecular Engineering, University of Notre Dame, Notre Dame, IN 46556, USA. E-mail: wschneider@nd.edu

^b Department of Chemistry and Biochemistry, University of Notre Dame, Notre Dame, IN 46556, USA

[†] Electronic supplementary information (ESI) available: DFT-computed lattice constants of hexagonal and orthorhombic M2P, and pure metals; band structure analyses; summary of adsorption energies at M3 and P1 sites on hexagonal and orthorhombic M2P and pure metal surfaces; vibrational frequencies of transition states for H-C₂H₃ on Pd₂P(001)-A; relaxed structures of hexagonal Pt₂P(001)-A,B and orthorhombic Pt₂P(010). Zenodo repository available at https://doi.org/ 10.5281/zenodo.6824056 contains the input files (INCAR, KPOINT) for VASP, and the full set of CONTCARs for all the structures discussed in the manuscript. See DOI: https://doi.org/10.1039/d2cy00602b

energies (either directly through adsorption/desorption steps or indirectly through Brønsted-Evans-Polanyi relationships), understanding trends in adsorption on metal phosphides is an important first step towards metal phosphide catalyst design for selective EDH. However, those trends may be sensitive to phosphide composition, bulk crystal structure, and even exposed facet.²³ The structural and compositional diversity of metal phosphides are substantial obstacles to interrogating metal phosphide chemistry in a consistent way.

There have been several attempts to examine general adsorption trends and/or catalytic behavior across metal phosphide surfaces using DFT.²⁴⁻²⁸ One common approach is to screen across metal phosphides of different stoichiometry and to select low energy or common facets. 24,25 The Bravais-Friedel-Donnay-Harker (BFDH) algorithm, which is based on morphology of crystal structures, is useful for identifying low energy surface facets.^{29,30} For example, Kibsgaard et al.²⁴ used BFDH to infer morphologically important facets (predicted to be common) of CoP, Co₂P, FeP, Fe₂P, Ni₂P and MoP as a basis for further analysis of hydrogen adsorption free energies $(\Delta G_{\rm H})$ of relevance to the hydrogen evolution reaction (HER). Another approach is to dope the screening element of interest into a fixed phosphide structure and observe the effect on adsorption energy.²⁵⁻²⁸ As a representative case, Partanen et al. 27,28 modeled Mg-, Mo-, Fe-, Co-, V- and Cu-doped Ni₃P₂-terminated Ni₂P(001) to look at variations in $\Delta G_{\rm H}$ with different dopants for HER. They predicted that thermodynamic stability and $\Delta G_{\rm H}$ vary substantially with the number and identity of dopants. This approach exploits consistent geometric features to extract composition-specific information. Extending either approach to EDH is challenged by the diversity of potential phosphide structures and facets and the greater number and complexity of EDH-relevant intermediates than HER.

Research to date suggests that metal-rich phosphides hold the most promise as EDH catalysts. 17-22 In this work, we use DFT models to explore the effect of geometric and chemical features on the adsorption energies of small hydrocarbons over the M2P metal-rich phosphides. We construct geometrically consistent representations of M₂P structure, M = Fe, Co, Ni, Cu, Mo, Ru, Rh, Pd, Ag and Pt including both hexagonal (Ni₂P, Fe₂P) and orthorhombic (Co₂P, Ru₂P) structures that are common to a subset of these materials. We construct a consistent series of close-packed planes, and explore adsorption of EDH fragments across surfaces. We compare across bulk and surface representations and across metal- and phosphorus-centered adsorption sites to figure out P participation in adsorbate-binding. We show that adsorption energies vary with composition of metal phosphides, adsorption sites, in particular metal vs. P sites. Lastly, we consider implications for EDH applications.

2 Computational details

Density functional theory (DFT) calculations were performed with the Vienna ab initio simulation package (VASP).31-33 Exchange-correlation energies were treated within the generalized gradient approximation (GGA)34 using the Perdew-Burke-Ernzerhof (PBE) functional. Bulk lattice parameters were computed at a plane wave cutoff of 520 eV and slab calculations with a wave cutoff of 400 eV. Ni, Fe, Co, Fe₂P and Co₂P were performed spin-polarized; in test calculations, we found Ni₂P to have a negligible magnetic moment. GGA-computed lattice parameters are summarized in Table S1.† Bulk hexagonal M₂P (space group P62m) consists of alternating M₃P₂ and M₃P₁ planes stacked along the [001] direction. Bulk orthorhombic M₂P (space group *Pnma*) has the same layer of M₂P stacked along the [001] direction. We chose the close-packed surface of the parent metals; Ni, Cu, Rh, Pd, Ag, Pt for fcc(111), Mo, Co and Ru for hcp(001), and bcc(110) for Fe. They were modeled with fivelayer slabs. On the other hand, hexagonal M2P(001)-A,B and orthorhombic (010) surfaces were modeled with six-layer slabs. For all metal and metal phosphide surfaces, we introduced a vacuum spacing of 15 Å. The bottom three layers were fixed at their bulk positions, and the remaining layers and adsorbates fully relaxed. (3×3) and (1×1) surface unit cells were employed for parent metal and M2P surfaces. Monkhorst-Pack grids³⁵ of $3 \times 3 \times 1$, $7 \times 7 \times 1$ and $7 \times 8 \times 1$ k-points were selected for metal surfaces, hexagonal M₂P(001) and orthorhombic M₂P(010).

Geometries were relaxed to minima using the conjugate gradient algorithm until forces on unconstrained atoms were less than 0.02 eV Å⁻¹. The adsorption energy (E_{ads}) is defined as

$$E_{\text{ads}} = E_{\text{total}} - E_{\text{slab}} - E_{\text{adsorbate}}$$
 (1)

Here, E_{total} is the total energy of the system with adsorbed species, E_{slab} is the total energy of the surface, and $E_{\text{adsorbate}}$ is the gas-phase energy of the adsorbate. The climbing image-nudged elastic band (CI-NEB) method was employed to determine the minimum energy paths and calculate the activation energies for surface reactions.36 The vibrational spectra were obtained by calculating the Hessian matrix with finite differences of 0.015 Å. Each transition state was verified to have a single imaginary frequency along the reaction coordinate. All atomic positions after geometry optimizations with corresponding energy profiles are provided in ESI.† To identify the amount of charge transfer between metal and P atoms, Bader charge analysis was employed. 37-39

3 Results and discussion

3.1 Bulk models

We created isostructural hexagonal and orthorhombic M2P series (M = Fe, Co, Ni, Cu, Mo, Ru, Rh, Pd, Ag, and Pt), shown in Fig. 1. Hexagonal M₂P is the equilibrium crystal structure of Ni₂P and Fe₂P, and orthorhombic M₂P is that of Co₂P and Ru₂P.^{40,41} To minimize effects arising from gross structural differences between the hexagonal and orthorhombic crystal structures, we focused on the close-packed flat surface terminations, including hexagonal (001) and orthorhombic

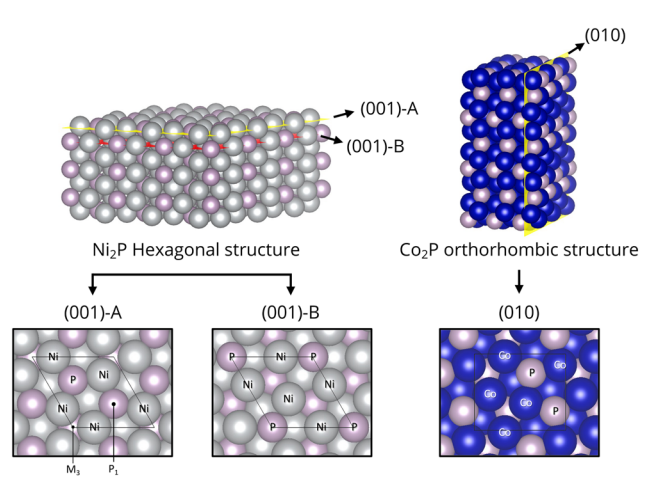


Fig. 1 Bulk hexagonal Ni₂P, and orthorhombic Co₂P structures and their facets. Ni, Co and P atoms are shown in gray, blue and lavender, and adsorption sites labeled on hexagonal (001)-A surface.

(010) facets (Fig. 1). We took two different terminations from hexagonal (001) because alternating planes of Ni₃P₂("A") and Ni₃P₁("B") are stacked along the [001] direction while orthorhombic (010) is the only facet along the [010] direction.

Fig. 2 reports computed formation energies relative to bulk metal and phosphorus $(E_f = E_{M_2P} - 2E_{M_{bulk}} - E_{P_{bulk}})$ of the orthorhombic and hexagonal M₂P structures. Here E_{M_2P} , $E_{M_{bulk}}$ and $E_{P_{bulk}}$ are the total energy of bulk M_2P , parent metal and red phosphorous, respectively. Formation energies are negative except for Cu₂P and Ag₂P. Formation energies of hexagonal (red circle) and orthorhombic (blue circle) are almost identical. We use hull distance to evaluate the stability of a compounds with respect to another phase or combination of phases. 42 The green data in Fig. 2 correspond

to the formation energies of the M2P phase on the convex hull if one exists and is neither hexagonal nor orthorhombic. If a stable M₂P phase is unknown, we computed formation energies of ground state structures of bounding compositions and report in Fig. 2 the energy of the tie line at M2P as unfilled green circles. 42,43 For example, a stable Mo₂P phase is unknown. We computed the formation energies of the known MoP (Mo/P = 1) and Mo₃P (Mo/P = 3) phases, constructed the tie line between the two, and report in Fig. 2 the energy of the tie line at Mo/P = 2. Thus, hexagonal and orthorhombic Pd₂P, Mo₂P, Rh₂P, Ag₂P and Pt₂P are thermodynamically unstable to phase separation, Pd₂P least so, and Pt₂P most so.

We performed Bader charge analysis on both hexagonal and orthorhombic bulk structures to quantify the electronic state changes with respect to elements and coordinations. Hexagonal M₂P contains tetrahedral (T) and square pyramidal (SP) metal sites as well as two inequivalent tetrakaidecahedral (TKD) P sites, which we label TKD1 and TKD2, respectively. Orthorhombic M2P also has T and SP metal sites, but a single P TKD. These sites are illustrated in Fig. 3.

Fig. 4a and b report computed Bader charges on metal and phosphorus sites in the hexagonal and orthorhombic structures, respectively. Despite the consistent stoichiometry, charges vary widely with composition; phosphorus charges vary from near +0.4e with the most electronegative metal (Pt) to -1.0e on the most electropositive (Mo). Metal charges vary proportionally and in the opposite direction. Results are generally consistent with electronegativity differences and computed-charge states of other phosphides. 15,44 Thus, it would be inappropriate to think of the metals as having a single formal charge across the series.

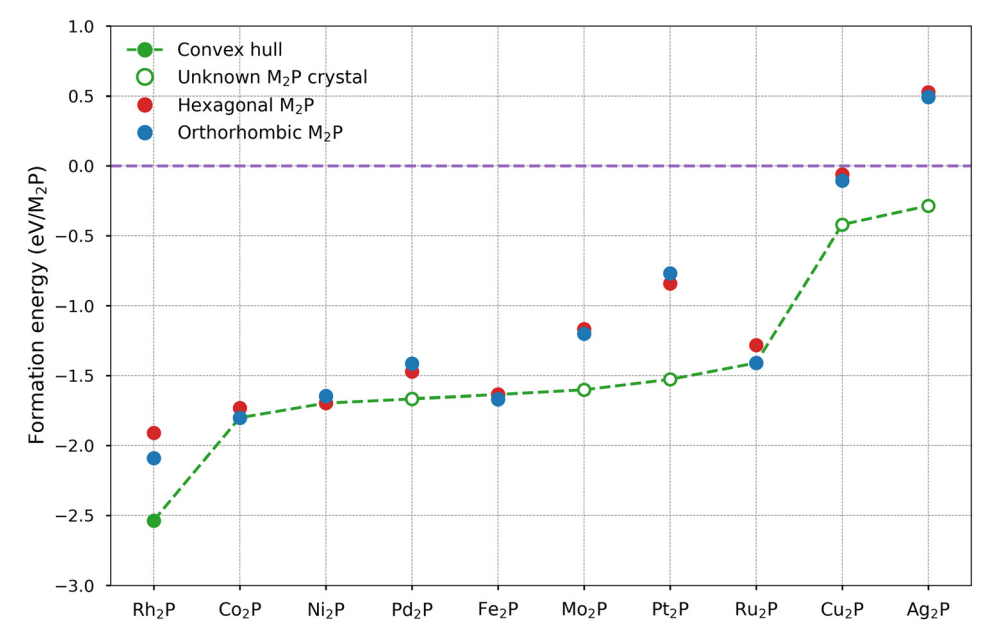


Fig. 2 Formation energies (E_f) of hexagonal (red) and orthorhombic (blue) M₂P structures. E_f of most stable M₂P structure if one exists (solid green), or energy of tie line between structures of bounding compositions (open green).

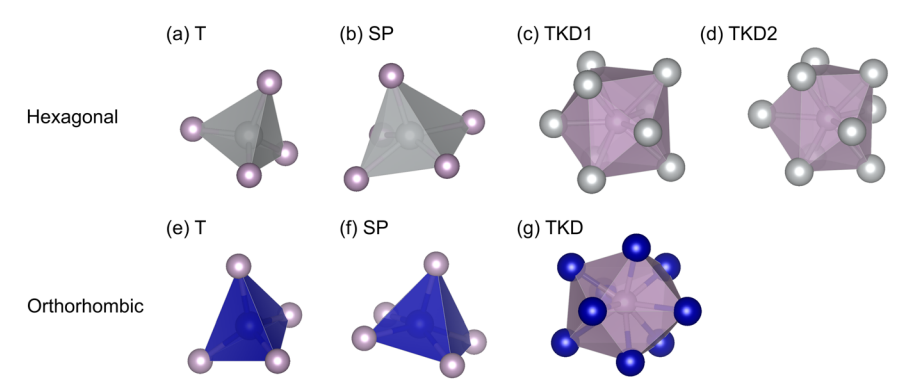


Fig. 3 Atomic coordinations of metal and P atoms in hexagonal Ni₂P ((a)-(d)) and orthorhombic Co₂P ((e)-(g)) structures. T and SP are tetrahedral and square pyramidal sites for metal atoms, respectively. TKD is tetrakaidecahedral site for P atoms. Ni, Co and P atoms are shown in gray, blue and lavender, respectively.

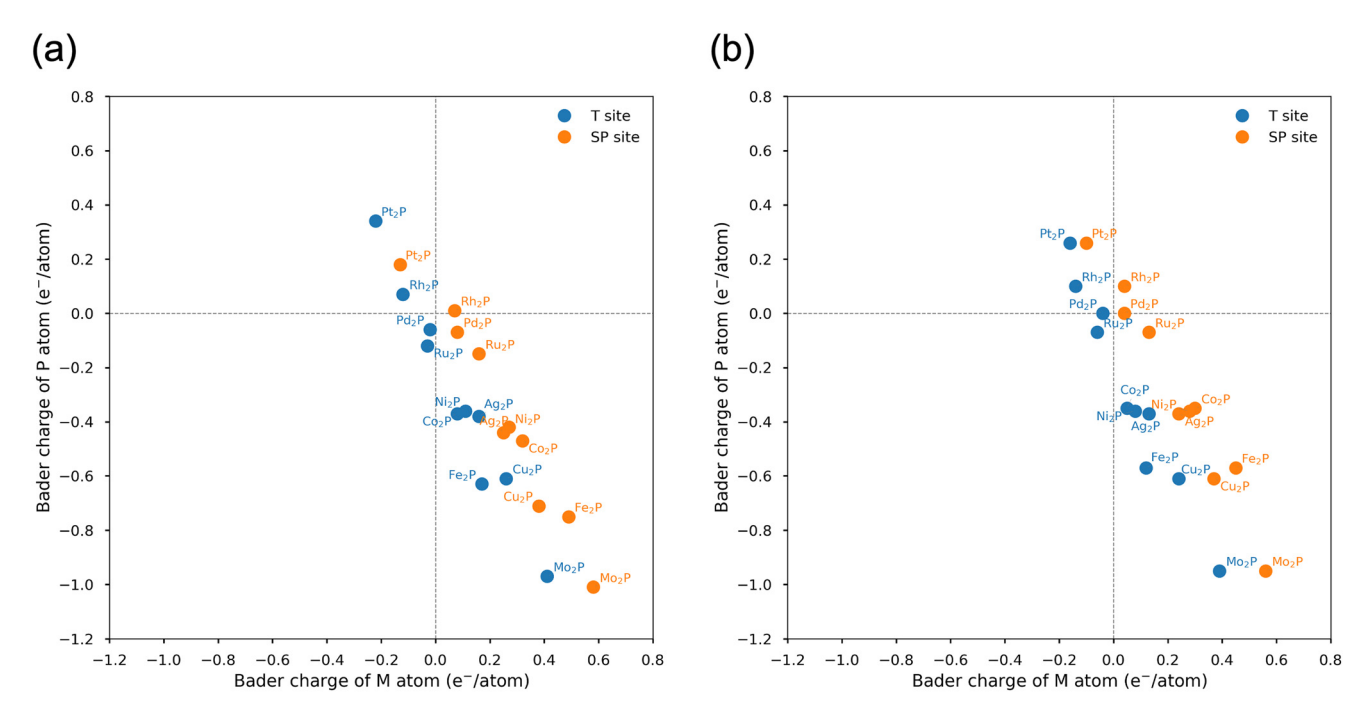


Fig. 4 Bader charge of metal and P atoms in (a) hexagonal and (b) orthorhombic M₂P bulk structures. Metal T and SP sites were compared to phosphorous TKD sites, respectively.

Trends are slightly sensitive to metal coordination numbers and essentially insensitive to bulk structure.

3.2 Metal and metal phosphide adsorption energies

We next cleaved and relaxed the bulk structures to generate the surfaces shown in Fig. 1. All surfaces save the Pt₂P case retained the same equilibrium structure. In the Pt₂P case, sublayer P atoms migrate to the surface and isolate surface Pt atoms, destroying the Pt₃ ensemble (shown in Fig. S1†). This instability is consistent with the large distance of the hypothetical Pt₂P structures above the tie line (Fig. 2). We thus excluded Pt₂P from adsorbate comparisons. Fig. S2† reports atom-projected densities of states of the remaining surfaces. Phosphorus p states are generally broad and low in energy. Interactions with P broadens and splits the metal d states, which dominate the states near the Fermi level for all compounds save Pd₂P, Cu₂P and Ag₂P. As with charges, DOS are generally insensitive to structure. Fig. S3† reports d band centers relative to the Fermi level for the M2P(001)-A surface vs. d band centers of the corresponding metal surfaces. Phosphorus incorporation results in a downward shift of d centers for almost all phosphides, especially pronounced for Cu₂P and Pd₂P. Shifts are generally insensitive to structure (Table S2†).

Given that electronic structure appears to be insensitive to bulk structure and local site coordination, we first consider adsorption chemistry on the hexagonal M₂P(001)-A facet. We

select H, CH₃, CH, and C as probes of saturated (sp³), unsaturated (sp) and carbonaceous adsorbates and compute adsorption at the M3 sites (shown in Fig. 1). We also compute adsorption on the corresponding site on the parent metal to assess the influence of P incorporation on adsorption. Adsorbates were placed above the center of the three-fold (M₃) site and relaxed. All relaxed structures are provided in the ESI.† The addition of adsorbates results in a general contraction in the trimeric metal ensemble (-0.28 Å $\leq \Delta d_{M-M}$ \leq -0.01 Å). In some cases, adsorbates relaxed away from the M₃ sites to 2-fold or 4-fold sites (e.g., C on Fe(110)). These cases were excluded from the analysis as well.

Fig. 5 reports parity plots of the binding energies on the phosphide surface vs. the metal. Energies span similar ranges on the metal and phosphide and are roughly linearly correlated but do not exhibit a consistent shift as might be expected from the d band center comparisons. Significant positive and negative deviations are evident, large enough to alter binding energy orderings. Binding energies on Ni₂P(001)-A and Pd₂P(001)-A are always less negative than on the parent metals. Pd₂P(001)-A is the most extreme outlier. P addition into Pd increases binding energies from 0.47 eV for CH₃ up to 1.97 eV for C. In contrast, P addition results in negative deviations on Co₂P(001)-A and Fe₂P(001)-A. On the other metal phosphides, deviations are adsorbates-specific. These deviations in binding energies from the parity line do not correlate with M3 ensemble size, lattice parameters, adsorbate-induced surface relaxation, or other geometric features. As shown in Fig. S4,† metal site adsorption energies roughly correlate with d band center shift, although again significant outliers are present.

Previous DFT calculations of EDH reaction paths on Ni₂P(001) reveal that surface P atoms do participate in some C-H bond cleavage steps. 17 This selective participation is related to the preference of sp² and sp³ C for P sites, which is computed to increase the activation energies of deep dehydrogenation steps over the bulk metal and thus to enhance ethylene selectivity. As shown in the inset of Fig. 6,

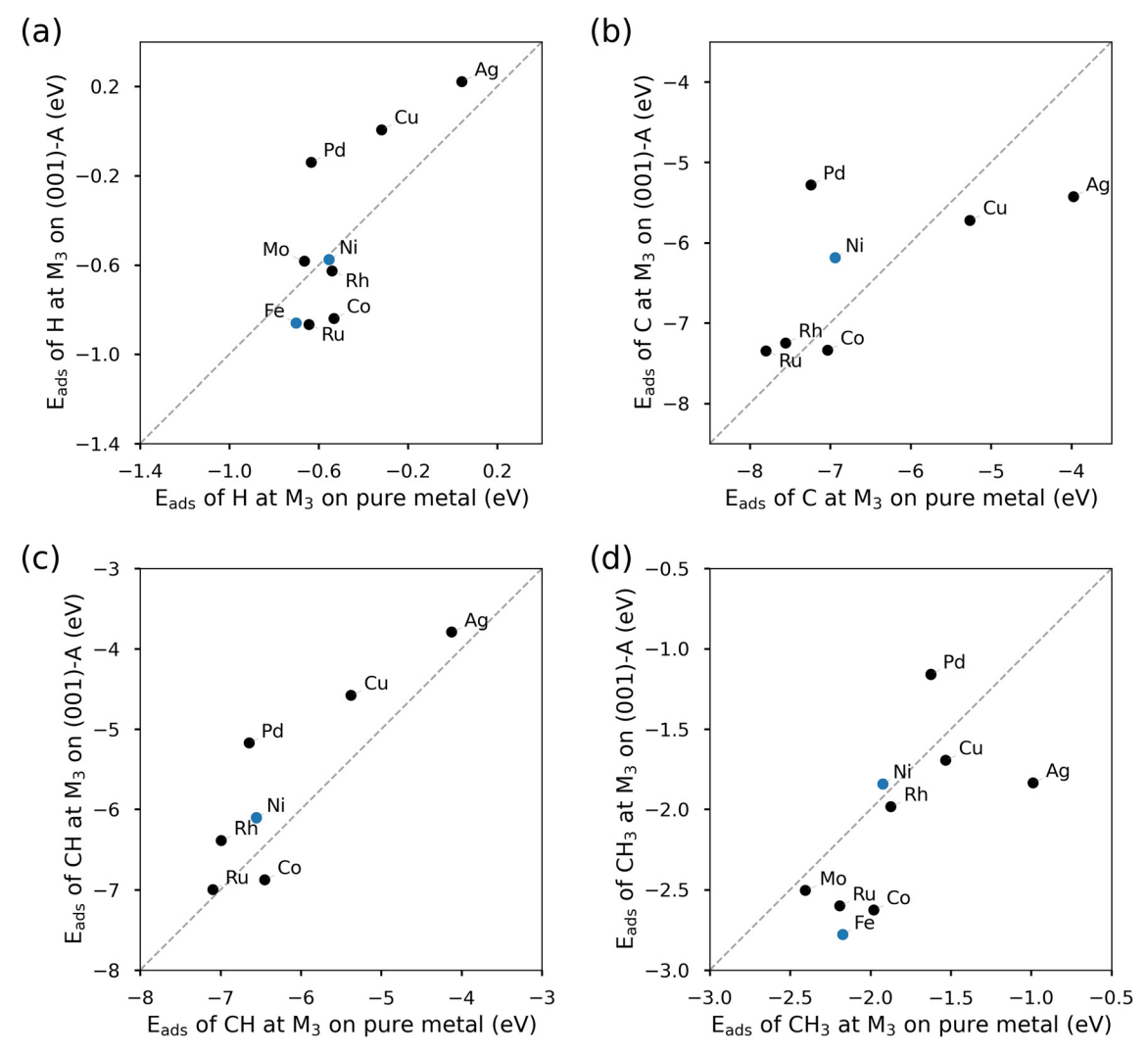


Fig. 5 Adsorption energies of (a) H, (b) C, (c) CH and (d) CH₃ on hexagonal M₂P(001)-A plotted against adsorption energies on the corresponding metals. Blue markers highlight compounds that are stable in the hexagonal M₂P structure.

Paper

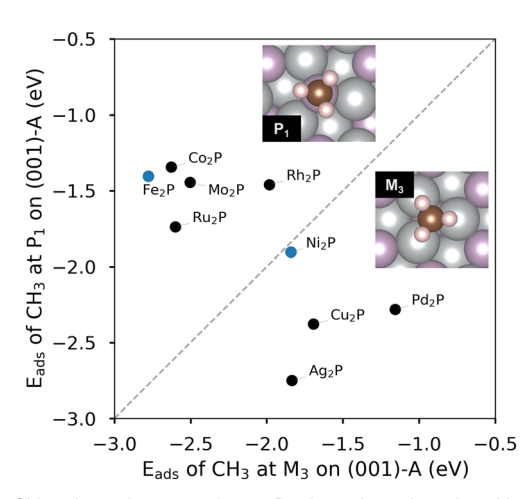


Fig. 6 CH₃ adsorption energies at P₁ sites plotted against M₃ sites on hexagonal M₂P(001)-A. Blue markers highlight compounds that are stable in the hexagonal M2P structure.

CH₃ can bind both in the three-fold metal hollow and atop P; binding energies on these two sites are nearly the same. 17 We performed similar comparisons using CH3 as a probe of metal vs. P preference across the M2P series. We relaxed CH3 at M3 and atop P sites (shown in the inset of Fig. 6) and compared adsorption energies. Resultant structures of P site binding are provided in ESI.† CH3 binding energies at atop P sites are plotted against M3 sites in Fig. 6. Binding energies are roughly anti-correlated, with earlier and less noble d block metals generally exhibiting stronger binding at metal than P sites. The P site is preferred for the later metals Cu₂P(001)-A, Pd₂P(001)-A and Ag₂P(001)-A, which are similarly the phosphides that have a large contribution of phosphorus p states at the Fermi level and low-lying metal d states (Fig. S3†). Phosphorus sites are thus expected, as with Ni₂P, to have a strong influence on C-H activation steps.

We repeated H, C, CH, CH₃ relaxation calculations at the M₃-centered sites on hexagonal M₂P(001)-B and orthorhombic M₂P(010) surfaces. In some cases, adsorbates (especially C

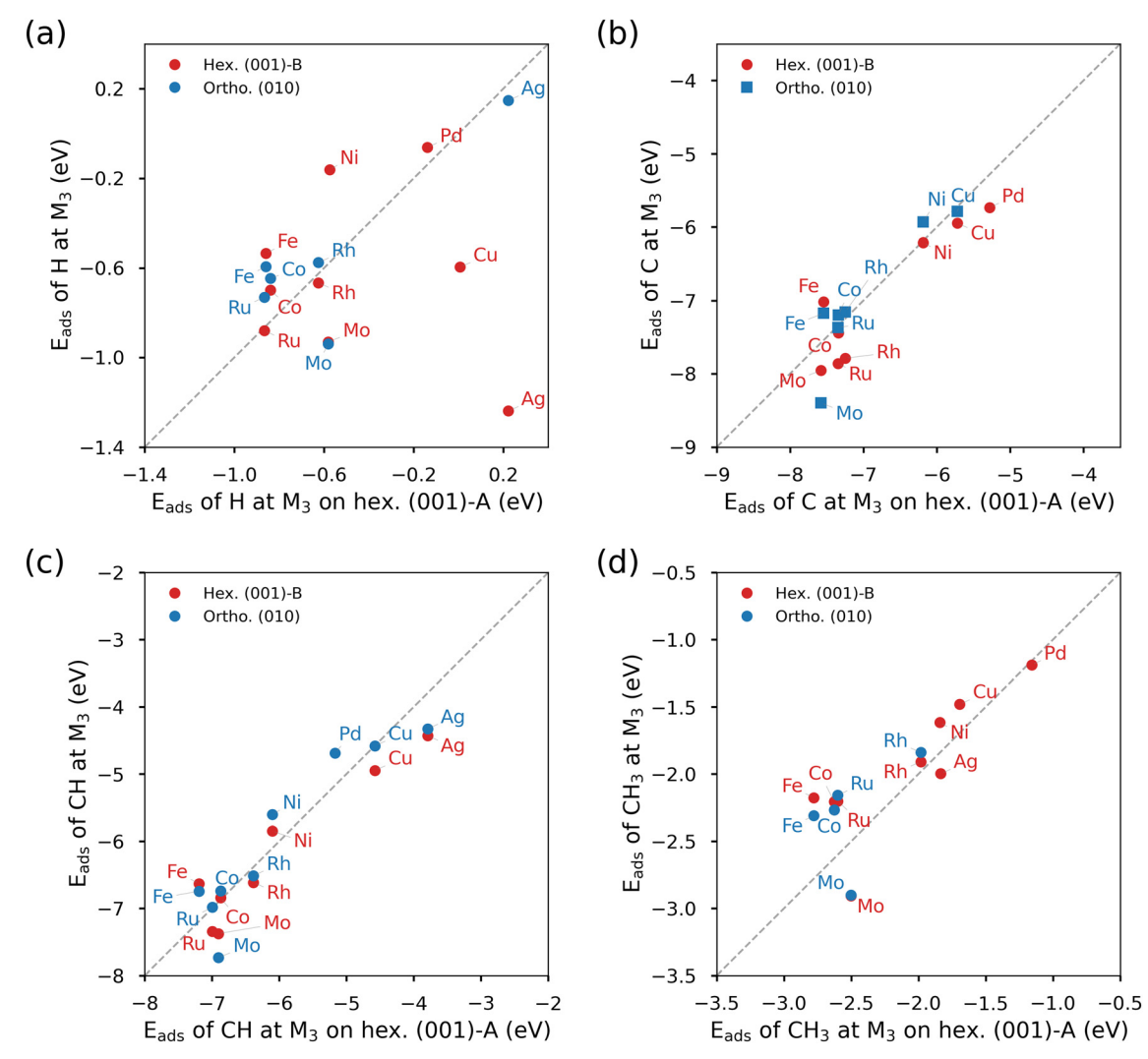


Fig. 7 Parity plots of (a) H, (b) C, (c) CH, and (d) CH₃ binding energies on hexagonal M₂P(001)-B and orthorhombic M₂P(010) M-centered sites vs. hexagonal M2P(001)-A M-centered sites.

atoms) move away from M₃ sites to atop or bridge sites or move subsurface. These cases were excluded from our energy comparisons to assure consistency. $E_{\rm ads}$ are summarized in ESI† Tables S4-S6. Fig. 7a reports H adsorption energies on the $M_2P(001)$ -B and $M_2P(010)$ surfaces vs. adsorption energies on M₂P(001)-A; panels b-d report similar comparisons for C, CH, CH₃, respectively. The results in panels b-d show that hydrocarbon binding energies at metal sites are generally insensitive both to bulk structure and surface termination. Largest deviations from parity are 0.83 eV, and are small relative to variations with metal. In contrast, and as highlighted in panel a, H binding energies evidence greater sensitivity to structure. Deviations from parity increase from the earlier to the later metals. The most dramatic example is H binding on the Ag₂P(001) A and B facets; these differences do not appear to have an origin in differences in structure (Fig. S5 in ESI†). Missing points in Fig. 7, including H on orthorhombic Ni₂P, Pd₂P and Cu₂P, correspond to cases in which adsorbates migrate from the M3 to other sites or subsurface.

We also compared M_3 and P-site binding energies across the hexagonal $M_2P(001)$ -B and orthorhombic $M_2P(010)$ surfaces (ESI† Table S7). Fig. 8 plots adsorption energies at P sites against M_3 sites across all metals and structures. Spontaneous migration of CH_3 from M_3 to atop M or M-M bridge sites were observed especially on orthorhombic (010). Those cases were excluded in this analysis. General trends are consistent with Fig. 6. Structure has a large effect for some metals, prominent among them Fe.

3.3 Implication for EDH catalyst

The results above highlight large scale trends in expected reactivity of metal-rich phosphides and the varying extent of participation of P in surface chemistry. Next we leverage

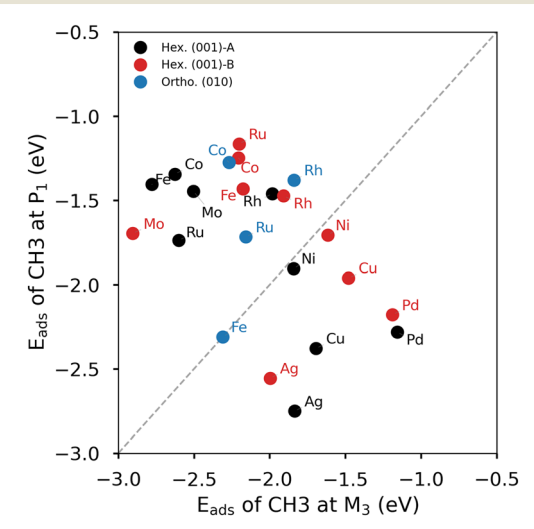


Fig. 8 Comparison of adsorption site preference of CH_3 at M-centered sites on hexagonal $M_2P(001)$ -A,B and orthorhombic $M_2P(010)$.

those insights and results towards selection of EDH candidate materials.

Prior work suggests that the EDH ethylene selectivity and coking resistance imparted by converting Ni into Ni₂P can be traced to the weaker binding of small hydrocarbons on Ni₂P than Ni and the preference of sp² and sp³ C centers for P sites.17 We selected C and CH as binding energy probes because they are common fragments arising from C-C cleavage of C2 species. Fig. 9 compares the adsorption energies of C and CH on hexagonal M2P(001)-A to those on Pt(111) and Ni₂P(001)-A, chosen as representative metallic (and quickly deactivating) and higher performing phosphide EDH catalysts. Data are taken from Fig. 5. Fragment binding energies are greater on most of the other phosphides than on Ni₂P(001)-A and in many cases are even comparable to binding energies on Pt(111). The exceptions include the late metal phosphides Cu₂P(001)-A, Pd₂P(001)-A and Ag₂P(001)-A. Further, and as shown in Fig. 6, CH₃ prefers phosphide over metal sites on these late metal phosphides, as was found to be an important feature underlying the EDH activity on Ni₂P. Thus, the Cu₂P, Pd₂P, and Ag₂P (001) facets share many of the same favorable EDH features as does Ni₂P.

Metal-rich Cu–P and Ag–P phases are yet to be reported, 45,46 consistent with the large distance of the bulk M_2P compounds above the formation energy hulls (Fig. 2). In contrast, several metal-rich Pd phosphides are known, including Pd_5P_2 , Pd_3P and Pd_6P , $^{47-50}$ consistent with the short distance of Pd_2P above the hull. Thus, we chose Pd_2P for further investigation.

The difference between ethylene desorption $(C_2H_4^* \rightarrow$ $C_2H_4(g) + *$ and ethylene dehydrogenation $(C_2H_4^* + *)$ C₂H₃* + H*) energies is a common descriptor for EDH selectivity. We chose C2H4 at atop Pd (the lowest energy) and Pd-P bridge (local minimum) sites as initial states. Then we sampled an H atom around the C2H3 at the lowest energy site (P1) as well as local minima sites (Pd-Pd bridge, Pd-P bridge) to find co-adsorption configurations of C₂H₃* and H* (final states). Those initial and final states were used as endpoints for reaction pathways for activation of H-C₂H₃*; the three different ethylene dehydrogenation pathways obtained from this analysis are shown in Fig. 10. C-H bond cleavage takes place at the Pd₃ site in pathway 1 and across the Pd-P bridge in pathway 2. After C-H bond cleavage, C₂H₃ diffuses to a Pd-P bridge site and H remains at the Pd-Pd bridge site in pathway 1 while dissociated H and C2H3 rotate slightly to reach their favored adsorption configurations in pathway 2. Energy differences between the two transition states are about 0.38 eV. In pathway 3, C₂H₄ starts at a slightly energy Pd-P bridge site. Similar to pathway 2, the C-H bond cleaves across a Pd-P bridge and H migrates to a Pd-Pd bridge site. Ethylene activation energies across all these pathways greatly exceed the ethylene desorption energy.

We repeated the same calculations on hexagonal Fe₂P(001)-A and Ni₂P(001)-A as contrasts to Pd₂P(001)-A. Fe₂P

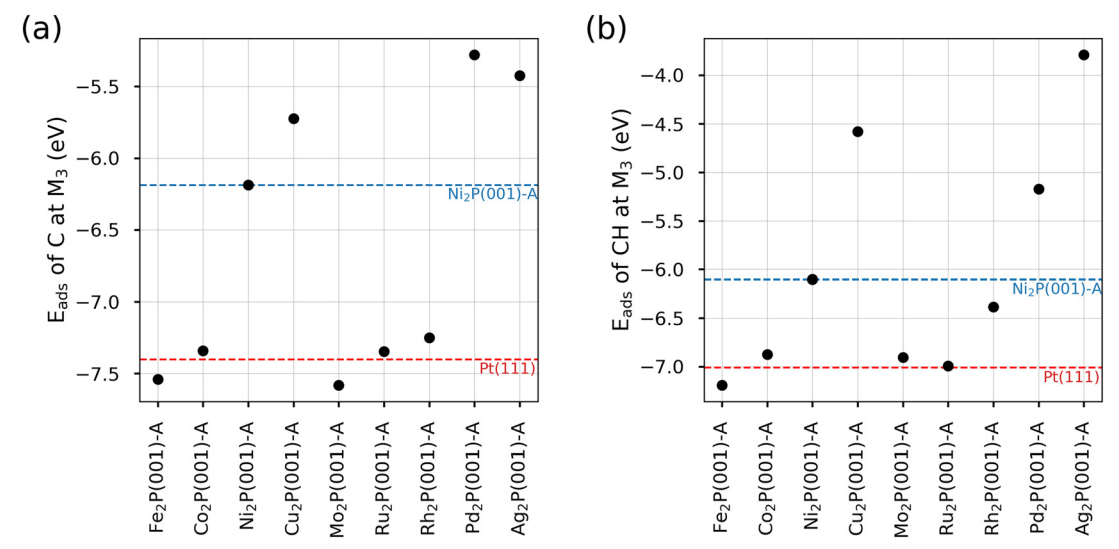


Fig. 9 Comparison of adsorption energies of (a) C and (b) CH over hexagonal M₂P(001)-A to those over Pt(111) (red dashed line) and Ni₂P(001)-A (blue dashed line).

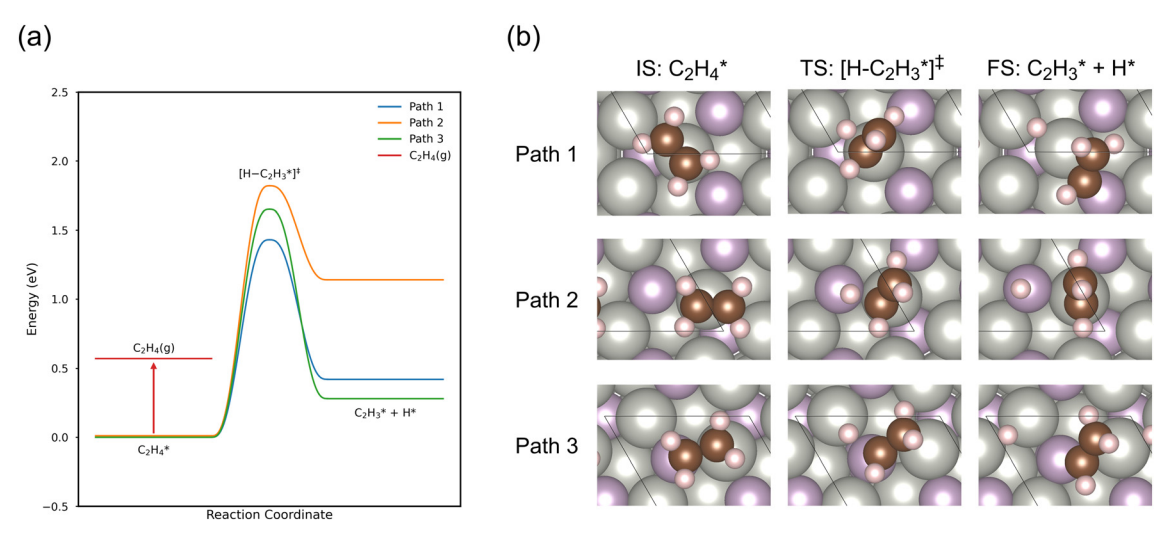


Fig. 10 (a) Comparison of three possible ethylene dehydrogenation pathways vs. ethylene desorption on hexagonal Pd₂P(001)-A. (a) Energy profiles of each pathway on Pd₂P(001)-A. (b) Geometric structures of initial state (IS), transition state (TS) and final state (FS) of three possible ethylene dehydrogenation pathways on Pd₂P(001)-A.

strongly binds adsorbates and has a strong preference to bind those adsorbates at metal sites, opposite the adsorption characteristics of Pd₂P. On the other hand, the characteristics of Ni₂P place it in the middle between Fe₂P and Pd₂P. Ethylene dehydrogenation energy profiles and geometric structures computed on the (001)-A facets are summarized in Fig. S6 and S7 of the ESI.† Due to the strong affinity of an Fe site for adsorbates, bond breaking takes place preferentially at Fe₂P metal sites (Fig. S7a†) with very small barriers; further; product ethylene is strongly surface-bound (Fig. S6a†). Ethylene dehydrogenation is more highly activated and ethylene desorption more accessible on Ni₂P(001)-A (Fig. S7b†), and both Ni or P sites potentially contribute to undesired C-H cleavage (Fig. S6b†). Those undesired pathways become even less favorable on Pd₂P, while ethylene desorption becomes even readier (Fig. S6b and c†). These calculations reinforce inferences from the C and CH binding energy trends, that the predicted EDH selectivity will follow $Pd_2P > Ni_2P \gg Fe_2P$.

Thus, results suggest that the Pd phosphides as potential candidates for selective EDH. Literature observations support this prediction. Pd phosphides have recently been explored for the selective dehydrogenation of hydrocarbons. 48-50 Sampath and Flaherty⁵⁰ in particular used temperature programmed reaction (TPR) and reactive molecular beam scattering (RMBS) to compare C₆H₁0 dehydrogenation over Pd and metal-rich Pd₃P phosphide. Selectivity to C₆H₆ is much greater over the Pd phosphide than Pd. Further, RMBS results suggest the phosphide to be more resistant to over dehydrogenation than is the metal.

4 Conclusions

Computational screening is a powerful technique for identifying new solid catalysts with desirable activity and selectivity. Metal phosphides are promising candidates for catalytic reactions involving C-H activation, but screening across metal phosphides is complicated by the large compositional and structural spaces as well as evidence that both metal and phosphorous sites participate in catalysis and contribute to observed selectivity. As a simple strategy to overcome some of these challenges, here we explore the surface chemistry of a series of isostructural metal-rich phosphides, some of which are stable compounds on the respective phase diagrams and some of which lie above known formation energy hulls. We compare a series of probe molecule bindings across a structurally consistent series of surface facets. Results are sensitive to metal but insensitive to structure, suggesting that the approach provides at least qualitative guidance in choice of phosphide for ethylene dehydrogenation. Analysis points to a metal-rich Pd phosphide as having desirable surface-chemical properties for selective EDH, a prediction at least qualitatively consistent with literature observation. While precise predictions clearly will be sensitive to precise structures and compositions, the approach offers an efficient first screen for phosphides and potentially other two-component systems (sulfides, nitrides, carbides) of interest for catalysis.

Conflicts of interest

There are no conflicts to declare.

Acknowledgements

We acknowledge financial support provided by the National Science Foundation Engineering Research Centers Program under Cooperative Agreement no. EEC-1647722, which funds the Center for Innovative and Strategic Transformations of Alkane Resources, CISTAR. CISTAR collaborators, in particular Jason Hicks and Jessica Muhlenkamp, are gratefully acknowledged. Computing resources and technical support for this work were provided by the Notre Dame Center for Research Computing.

References

- 1 P. C. A. Bruijnincx and B. M. Weckhuysen, Shale Gas Revolution: An Opportunity for the Production of Biobased Chemicals?, *Angew. Chem., Int. Ed.*, 2013, 52, 11980–11987.
- 2 E. E. Stangland, Shale Gas Implications for C2-C3 Olefin Production: Incumbent and Future Technology, Annu. Rev. Chem. Biomol. Eng., 2018, 9, 341–364.
- 3 J. J. H. B. Sattler, J. Ruiz-Martinez, E. Santillan-Jimenez and B. M. Weckhuysen, Catalytic Dehydrogenation of Light Alkanes on Metals and Metal Oxides, *Chem. Rev.*, 2014, **114**, 10613–10653.

- 4 National Academies of Sciences, E., Studies, D., Technology, B. and J. Alper, *The Changing Landscape of Hydrocarbon Feedstocks for Chemical Production: Implications for Catalysis: Proceedings of a Workshop*, National Academies Press, 2016.
- 5 W. U. S. Wilczewski, *Independent Statistics and Analysis*, Energy Information Administration – EIA, 2015, https://www.eia.gov/todayinenergy/detail.php?id=19771.
- 6 T. Ridha, Y. Li, E. Gençer, J. Siirola, J. Miller, F. Ribeiro and R. Agrawal, Valorization of Shale Gas Condensate to Liquid Hydrocarbons through Catalytic Dehydrogenation and Oligomerization, *Processes*, 2018, **6**, 139.
- 7 A. Hook, J. D. Massa and F. E. Celik, Effect of Tin Coverage on Selectivity for Ethane Dehydrogenation over Platinum— Tin Alloys, *J. Phys. Chem. C*, 2016, **120**, 27307–27318.
- 8 V. Galvita, G. Siddiqi, P. Sun and A. T. Bell, Ethane dehydrogenation on Pt/Mg(Al)O and PtSn/Mg(Al)O catalysts, *J. Catal.*, 2010, 271, 209–219.
- 9 J. Wu, Z. Peng and A. T. Bell, Effects of composition and metal particle size on ethane dehydrogenation over $Pt_xSn_{100-x}/Mg(Al)O$ (70 $\leq x \leq 100$), *J. Catal.*, 2014, 311, 161–168.
- 10 V. J. Cybulskis, B. C. Bukowski, H.-T. Tseng, J. R. Gallagher, Z. Wu, E. Wegener, A. J. Kropf, B. Ravel, F. H. Ribeiro, J. Greeley and J. T. Miller, Zinc Promotion of Platinum for Catalytic Light Alkane Dehydrogenation: Insights into Geometric and Electronic Effects, ACS Catal., 2017, 7, 4173–4181.
- 11 E. C. Wegener, Z. Wu, H.-T. Tseng, J. R. Gallagher, Y. Ren, R. E. Diaz, F. H. Ribeiro and J. T. Miller, Structure and reactivity of Pt-In intermetallic alloy nanoparticles: Highly selective catalysts for ethane dehydrogenation, *Catal. Today*, 2018, 299, 146–153.
- 12 Y. Bonita, T. P. O'Connell, H. E. Miller and J. C. Hicks, Revealing the Hydrogenation Performance of RuMo Phosphide for Chemoselective Reduction of Functionalized Aromatic Hydrocarbons, *Ind. Eng. Chem. Res.*, 2019, 58, 3650–3658.
- 13 Y. Pei, Y. Cheng, J. Chen, W. Smith, P. Dong, P. M. Ajayan, M. Ye and J. Shen, Recent developments of transition metal phosphides as catalysts in the energy conversion field, J. Mater. Chem. A, 2018, 6, 23220–23243.
- 14 D. J. Rensel, S. Rouvimov, M. E. Gin and J. C. Hicks, Highly selective bimetallic FeMoP catalyst for C-O bond cleavage of aryl ethers, *J. Catal.*, 2013, **305**, 256–263.
- 15 D. J. Rensel, J. Kim, V. Jain, Y. Bonita, N. Rai and J. C. Hicks, Composition-directed Fe_xMo_{2-x}P bimetallic catalysts for hydrodeoxygenation reactions, *Catal. Sci. Technol.*, 2017, 7, 1857–1867.
- 16 A. Cho, J. Shin, A. Takagaki, R. Kikuchi and S. T. Oyama, Ligand and Ensemble Effects in Bimetallic NiFe Phosphide Catalysts for the Hydrodeoxygenation of 2-Methyltetrahydrofuran, *Top. Catal.*, 2012, 55, 969–980.
- J. Ko, J. A. Muhlenkamp, Y. Bonita, N. J. LiBretto, J. T. Miller, J. C. Hicks and W. F. Schneider, Experimental and Computational Investigation of the Role of P in Moderating Ethane Dehydrogenation Performance over Ni-Based Catalysts, *Ind. Eng. Chem. Res.*, 2020, 59, 12666–12676.

- 18 J. A. Muhlenkamp, N. J. LiBretto, J. T. Miller and J. C. Hicks, Ethane dehydrogenation performance and high temperature stability of silica supported cobalt phosphide nanoparticles, Catal. Sci. Technol., 2022, 12, 976-985.
- 19 Y. Xu, H. Sang, K. Wang and X. Wang, Catalytic dehydrogenation of isobutane in the presence of hydrogen over Cs-modified Ni₂P supported on active carbon, Appl. Surf. Sci., 2014, 316, 163-170.
- 20 Y. Xu, X. Wang and R. Lv, Interaction between Cs and Ni₂P/ SiO₂ for enhancing isobutane dehydrogenation in the presence of hydrogen, React. Kinet., Mech. Catal., 2014, 113, 393-406.
- 21 Y. Yao, M. Zuo, H. Zhou, J. Li, H. Shao, T. Jiang, X. Liao and S. Lu, One-Pot Preparation of Ni2P/γ-Al2O3 Catalyst for Dehydrogenation of Propane to Propylene, ChemistrySelect, 2018, 3, 10532-10536.
- 22 Q. Zhu, H. Zhang, S. Zhang, G. Wang, X. Zhu and C. Li, Dehydrogenation of Isobutane over a Ni-P/SiO2 Catalyst: Effect of P Addition, Ind. Eng. Chem. Res., 2019, 58, 7834-7843.
- 23 S. T. Oyama, T. Gott, H. Zhao and Y.-K. Lee, Transition metal phosphide hydroprocessing catalysts: A review, Catal. Today, 2009, 143, 94-107.
- 24 J. Kibsgaard, C. Tsai, K. Chan, J. D. Benck, J. K. Nørskov, F. Abild-Pedersen and T. F. Jaramillo, Designing an improved transition metal phosphide catalyst for hydrogen evolution using experimental and theoretical trends, Energy Environ. Sci., 2015, 8, 3022-3029.
- 25 M. Fields, C. Tsai, L. D. Chen, F. Abild-Pedersen, J. K. Nørskov and K. Chan, Scaling Relations for Adsorption Energies on Doped Molybdenum Phosphide Surfaces, ACS Catal., 2017, 7, 2528-2534.
- 26 R. B. Wexler, J. M. P. Martirez and A. M. Rappe, Chemical Pressure-Driven Enhancement of the Hydrogen Evolving Activity of Ni2P from Nonmetal Surface Doping Interpreted via Machine Learning, J. Am. Chem. Soc., 2018, 140, 4678-4683.
- 27 L. Partanen, M. Hakala and K. Laasonen, Hydrogen adsorption trends on various metaldoped Ni2P surfaces for optimal catalyst design, Phys. Chem. Chem. Phys., 2019, 21, 184-191.
- 28 L. Partanen, S. Alberti and K. Laasonen, Hydrogen adsorption trends on two metal-doped Ni2P surfaces for optimal catalyst design, Phys. Chem. Chem. Phys., 2021, 23, 11538-11547.
- 29 R. Docherty, K. Roberts and E. Dowty, Morang A computer program designed to aid in the determinations of crystal morphology, Comput. Phys. Commun., 1988, 51, 423-430.
- 30 R. Docherty, G. Clydesdale, K. J. Roberts and P. Bennema, Application of Bravais-Friedel-Donnay-Harker, attachment energy and Ising models to predicting and understanding the morphology of molecular crystals, J. Phys. D: Appl. Phys., 1991, 24, 89-99.
- 31 G. Kresse and J. Hafner, Ab initiomolecular dynamics for liquid metals, Phys. Rev. B: Condens. Matter Mater. Phys., 1993, 47, 558-561.

- 32 G. Kresse and J. Hafner, Norm-conserving and ultrasoft pseudopotentials for first-row and transition elements, J. Phys.: Condens. Matter, 1994, 6, 8245-8257.
- 33 G. Kresse and J. Furthmüller, Efficient iterative schemes for ab initio total-energy calculations using a plane-wave basis set, Phys. Rev. B: Condens. Matter Mater. Phys., 1996, 54, 11169-11186.
- 34 J. P. Perdew, K. Burke and M. Ernzerhof, Generalized Gradient Approximation Made Simple, Phys. Rev. Lett., 1996, 77, 3865-3868.
- 35 H. J. Monkhorst and J. D. Pack, Special points for Brillouinzone integrations, Phys. Rev. B: Solid State, 1976, 13, 5188-5192.
- 36 G. Henkelman, B. P. Uberuaga and H. Jónsson, A climbing image nudged elastic band method for finding saddle points and minimum energy paths, J. Chem. Phys., 2000, 113, 9901-9904.
- 37 G. Henkelman, A. Arnaldsson and H. Jónsson, A fast and robust algorithm for Bader decomposition of charge density, Comput. Mater. Sci., 2006, 36, 354-360.
- 38 E. Sanville, S. D. Kenny, R. Smith and G. Henkelman, Improved grid-based algorithm for Bader charge allocation, J. Comput. Chem., 2007, 28, 899-908.
- 39 W. Tang, E. Sanville and G. Henkelman, A grid-based Bader analysis algorithm without lattice bias, J. Phys.: Condens. Matter, 2009, 21, 084204.
- 40 J. Kolny-Olesiak, Recent Advances in the Colloidal Synthesis of Ternary Transition Metal Phosphides, Z. Naturforsch. A, 2019, 74, 709-719.
- 41 R. Fruchart, A. Roger and J. P. Senateur, Crystallographic and Magnetic Properties of Solid Solutions of the Phosphides M2P, M = Cr, Mn, Fe, Co, and Ni, J. Appl. Phys., 1969, 40, 1250-1257.
- 42 J. Ma, V. I. Hegde, K. Munira, Y. Xie, S. Keshavarz, D. T. Mildebrath, C. Wolverton, A. W. Ghosh and W. H. Butler, Computational investigation of half-Heusler compounds for spintronics applications, Phys. Rev. B, 2017, 95, 024411.
- 43 C. J. Bartel, A. Trewartha, Q. Wang, A. Dunn, A. Jain and G. Ceder, A critical examination of compound stability predictions from machine-learned formation energies, npj Comput. Mater., 2020, 6, 97.
- 44 Y. He and S. Laursen, The surface and catalytic chemistry of the first row transition metal phosphides in deoxygenation, Catal. Sci. Technol., 2018, 8, 5302-5314.
- 45 J. E. Saal, S. Kirklin, M. Aykol, B. Meredig and C. Wolverton, Materials Design and Discovery with High-Throughput Density Functional Theory: The Open Quantum Materials Database (OQMD), JOM, 2013, 65, 1501-1509.
- 46 S. Kirklin, J. E. Saal, B. Meredig, A. Thompson, J. W. Doak, M. Aykol, S. Rühl and C. Wolverton, The Open Quantum Materials Database (OQMD): assessing the accuracy of DFT formation energies, npj Comput. Mater., 2015, 1, 15010.
- 47 L. B. Belykh, N. I. Skripov, L. N. Belonogova, V. A. Umanets and F. K. Schmidt, Synthesis, properties, and activity of nanosized palladium catalysts modified with elemental phosphorus for hydrogenation, Kinet. Catal., 2010, 51, 42 - 49.

- 48 L. B. Belykh, N. I. Skripov, T. P. Sterenchuk, K. L. Gvozdovskaya, S. B. Sanzhieva and F. K. Schmidt, Pd-P nanoparticles as active catalyst for the hydrogenation of acetylenic compounds, *J. Nanopart. Res.*, 2019, 21, 198.
- 49 Y. Liu, A. J. McCue, C. Miao, J. Feng, D. Li and J. A. Anderson, Palladium phosphide nanoparticles as highly selective catalysts for the selective hydrogenation of acetylene, *J. Catal.*, 2018, **364**, 406–414.
- 50 A. Sampath and D. W. Flaherty, Effects of phosphorus addition on selectivity and stability of Pd model catalysts during cyclohexene dehydrogenation, *Catal. Sci. Technol.*, 2020, **10**, 993–1005.
- 51 J. Ko, H. Ma and W. F. Schneider, Kinetic Origins of High Selectivity of Metal Phosphides for Ethane Dehydrogenation, *Ind. Eng. Chem. Res.*, 2022, **61**, in press.